

## Full Length Article

Molecular simulation of adsorption and diffusion behavior of CO<sub>2</sub> in pyrophylliteChunquan Li <sup>a</sup>, Shiqi Liu <sup>a,b,\*</sup>, Huiquan Tian <sup>c</sup>, Jiaxin Liang <sup>a</sup>, Yongbing Li <sup>d</sup><sup>a</sup> School of Earth Sciences and Engineering, Sun Yat-sen University, Guangzhou 510275, China<sup>b</sup> Southern Marine Science and Engineering Guangdong Laboratory (Zhuhai), Zhuhai 519080, China<sup>c</sup> School of Geography and Land Engineering, Yuxi Normal University, Yuxi 653100, China<sup>d</sup> Key Laboratory of Computational Geodynamics, University of Chinese Academy of Sciences, Beijing 100049, China

## ARTICLE INFO

## ABSTRACT

**Keywords:**  
CO<sub>2</sub>  
Pyrophyllite  
Adsorption  
Diffusion  
Water content  
Molecular simulation

Understanding the microscopic process of adsorption and diffusion of CO<sub>2</sub> in clay minerals is important for geological storage of CO<sub>2</sub>. In this study, Grand Canonical Monte Carlo (GCMC) and Molecular Dynamics (MD) simulations are used to obtain the adsorption and diffusion behavior of CO<sub>2</sub> in pyrophyllite slit pores. The influence of split pore size, temperature, pressure, and water content were analyzed in detail. The adsorption characteristics of CO<sub>2</sub> in pyrophyllite were revealed by discussing the distribution of CO<sub>2</sub> density profile, adsorption capacity, isosteric heat of adsorption, interaction energy, mean square displacement, self-diffusion coefficient, and molecular orientation distribution. It shows that the excess adsorption isotherm of CO<sub>2</sub> in pyrophyllite slit pores demonstrate significant supercritical adsorption characteristics. Surface attractions originating from both pore walls overlap in the middle of pore, leading to an enhanced adsorption capacity of CO<sub>2</sub> in pyrophyllite slit pores when pore aperture is lower than 3 nm. In pyrophyllite pores, the presence of water has an enhancing effect on CO<sub>2</sub> adsorption when the water content is below 30 wt%. A maximum value of CO<sub>2</sub> adsorption amount is reached at the water content of 10 wt%, while negative growth occurs at 35 wt%. At low water content, water molecules form a weak adsorption layer due to the weak attraction of pyrophyllite to water. As water content increases, the self-diffusion coefficient of the CO<sub>2</sub> decreases, and the diffusion capacity decreases. The adsorption state of the CO<sub>2</sub> molecule on the mineral surface is primarily a parallel configuration, while the water molecule has no clear orientation. Our calculated results can provide guidance for further study of clay-water-adsorbate interface reaction of hydrophobic minerals.

## 1. Introduction

Industrial emissions and fossil fuel combustion are the main reasons for the increase of atmospheric carbon dioxide (CO<sub>2</sub>) concentrations over the past few years. To mitigate the global greenhouse effect and climate change, by focusing on the reduction of CO<sub>2</sub> in the atmosphere, carbon capture and storage (CCS) technology has been explored [1–3]. Underground geological storage has been regarded as the most achievable approach for the last step in the CCS chain [4–6], and adsorption is one of the major ways for geological storage [7]. The optional geological storage sites are unmineable coal seams, shale, depleted oil and gas reservoirs, and saline aquifers [8]. In coal seams, the mass of CO<sub>2</sub> adsorbed by coal is about 10% of the mass of the coal itself under geological conditions [9]. In shale reservoirs, the adsorbed gas accounts

for 20 ~ 80% of the total gas amount, and the contribution of clay minerals accounts for 45 ~ 60% [10,11]. In CO<sub>2</sub> capture, approximately 85% of CO<sub>2</sub> is captured by absorbents [12]. Due to the layered structure and specific surface area, clay minerals have a high adsorption capacity and can be used as natural adsorbents for CO<sub>2</sub> [13,14]. Under the condition of geological storage, CO<sub>2</sub> can enter the slit pores of clay minerals [15]. Pyrophyllite is a widely distributed layered silicate clay mineral with abundant slit pores [16,17], which is similar to montmorillonite in crystal structure and does not contain cations between layers. From the perspective of mineralogy and geology, pyrophyllite mainly exists in metamorphic rocks and acidic volcanic rocks, usually coexisting with kaolinite and illite [18–20]. In some areas, the content of pyrophyllite is 14.7 ~ 17.4% in bauxite [21] and 20 ~ 51% in clay minerals [22]. So far, pyrophyllite has been widely applied in the treatment of

\* Corresponding author.

E-mail address: liushq8@mail.sysu.edu.cn (S. Liu).

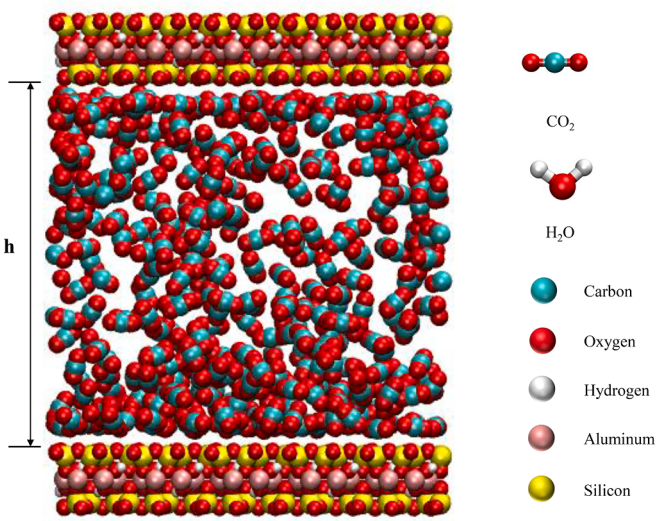


**Fig. 1.** The model of  $\text{CO}_2$ ,  $\text{H}_2\text{O}$  and pyrophyllite with the color scheme. The width of slit pore ( $h$ ) is the distance between two inner surfaces of clay sheets.

environmental pollutants due to its excellent adsorption performance [23]. There have been a lot of studies on the adsorption of metal cations in brine solution by pyrophyllite [23–26]. In addition, for some organic molecular compounds such as methylene blue, pyrophyllite also shows a strong adsorption capacity [27,28]. In depleted oil/gas reservoirs, previous studies have shown that hydrophobic pyrophyllite minerals show preferential adsorption to crude oil molecules [29]. On the other hand, the research on pyrophyllite adsorption gas mainly includes methane, gaseous nitrate, and nitrogen dioxide [30,31]. Recently, numerous researches on the geologic sequestration of  $\text{CO}_2$  have been investigated in clay minerals such as kaolinite and illite [32,33]. However, research on the adsorption of  $\text{CO}_2$  on pyrophyllite has not yet been carried out. To evaluate the  $\text{CO}_2$  adsorption of clay minerals more comprehensively, it is necessary to study the  $\text{CO}_2$  adsorption potential of pyrophyllite under different geological conditions.

In previous  $\text{CO}_2$  adsorption simulation studies, most of them focused on expansive clay minerals such as montmorillonite, illite, chlorite, and kaolinite [7,10,34–36]. There are two main methods to study the adsorption characteristics of clay minerals: experiment and molecular simulation. In the experiment, the adsorption capacity and storage integrity of  $\text{CO}_2$  geological storage in sedimentary rocks were evaluated by studying the adsorption capacity of montmorillonite to  $\text{CO}_2$  under subcritical to supercritical conditions [37]. Due to the limitation of the scale of traditional methods, indoor gas adsorption experiments cannot provide more details about adsorption behavior. In comparison, through the combination of Monte Carlo and molecular dynamics simulation, the adsorption and diffusion mechanism of  $\text{CO}_2$  in clay minerals can be revealed at the micro-scale. Monte Carlo is a simulation method that obtains a solution by calculating the statistical ensemble average of random variables [38]. In a molecular simulation, it can be used to study the adsorption properties of gases in nanopores. Molecular dynamics simulation based on the equilibrium adsorption configuration obtained by the Monte Carlo method can further obtain the dynamic properties of particles, such as motion trajectories and spatial distribution. In the adsorption simulation, in addition to temperature, pressure, and clay layer spacing, the influence of water content in clay mineral (pre-adsorption water) should also be considered due to the existence of formation water [39]. The adsorption capacity of minerals is related to the interlayer charge and the chemical characteristics of the mineral interface. The basal surface of clay minerals can be categorized as gibbsite and siloxane surfaces according to their hydrophobicity. In nature, hydrophobic surfaces widely exist in clay minerals, such as kaolinite, which is a 1:1 layered silicate mineral. The upper and lower

surfaces of its single-layer structure are hydrophilic and hydrophobic, respectively. Previous studies have mainly investigated the adsorption capacity of  $\text{CO}_2$  in the nanopores of kaolinite with gibbsite surfaces [40–42]. Recently, researchers have found that the siloxane pores composed of hydrophobic surfaces of kaolinite have a weaker adverse effect on adsorption relative to the gibbsite pores with hydrophilic surfaces [43]. Due to the intricate distribution and interlayer structure of clay minerals in rocks, mixed-layer minerals can readily form between clay minerals with different substrate surface properties, such as illite-smectite, chlorite-smectite, and kaolinite-smectite [44–48]. For hydrophilic minerals such as montmorillonite, interlayer water molecules form a water film on the mineral surface and occupy numerous adsorption sites, reducing the amount of  $\text{CO}_2$  adsorption. For hydrophobic minerals such as pyrophyllite, the Density Functional Theory (DFT) and ab initio molecular dynamics simulation (AIMD) results show that the interaction between water molecules is stronger than that between the water molecule and the mineral surface, so multiple water molecules are easy to form clusters [49]. In addition, hydrophobicity is conducive to  $\text{CO}_2$  storage in the underground aquifer [29]. To reveal the effect of water content on  $\text{CO}_2$  adsorption, it is necessary to consider the different water content of hydrophobic mineral interlayer structures in molecular simulation.

In this study, the adsorption and diffusion behavior of  $\text{CO}_2$  in pyrophyllite slit pores are investigated by GCMC and MD methods. GCMC simulation can obtain isosteric heat of adsorption and gas adsorption amount. Dynamic properties such as radial distribution functions, self-diffusion coefficient, and density profile can be calculated using MD simulation. The effect of pore sizes, temperatures, pressures, and water contents are taken into account. The interaction energy, total and excess adsorption, adsorption phase density, isosteric heat, adsorption sites, mass density profile, and diffusion properties for  $\text{CO}_2$  are analyzed, respectively. This study can enhance the understanding of  $\text{CO}_2$  adsorption on clay minerals with siloxane pores. Furthermore, the influence of water content on  $\text{CO}_2$  adsorption can aid in developing a gas–water adsorption model at complex reservoir conditions. The results can provide molecular insights for gas adsorption in the CCS project.

## 2. Methods

### 2.1. Molecular model of pyrophyllite

Pyrophyllite is the simplest dioctahedral phyllosilicate with two tetrahedral sheets and one octahedral sheet. In this study, the unit cell of pyrophyllite is represented by  $\text{Al}_2\text{Si}_4\text{O}_{10}(\text{OH})_2$ . The crystal structure of pyrophyllite was taken from the X-ray diffraction studies [50,51]. The lattice parameters were listed in Table S1. Each simulation box consists of two pyrophyllite layers. The clay sheet size was approximately  $4.13 \times 4.48 \text{ nm}$  in the x-y plane consisting of  $6 \times 5 \times 1$  unit cells. Considering the influence of pore aperture, eight clay sheets varying from 1 nm to 8 nm were used in simulations, respectively. The aperture of slit pore ( $h$ ) was defined as the distance between two most inner clay surfaces. To explore the effect of water content on  $\text{CO}_2$  adsorption, water contents varying from 3 wt% to 40 wt% were considered in the simulations. Water content (wt%) was defined in Eq. (1):

$$\text{wt\%} = \frac{m_{\text{water}}}{m_{\text{adsorbent}}} \quad (1)$$

where  $m_{\text{water}}$  and  $m_{\text{adsorbent}}$  represent the mass of water and pyrophyllite [52]. Fig. 1 shows a snapshot of simulation configuration and small molecules using in this study. All the snapshots of simulations were visualized by visual molecular dynamics (VMD) software [53].

### 2.2. Force field

CLAYFF force field was employed to characterize pyrophyllite,

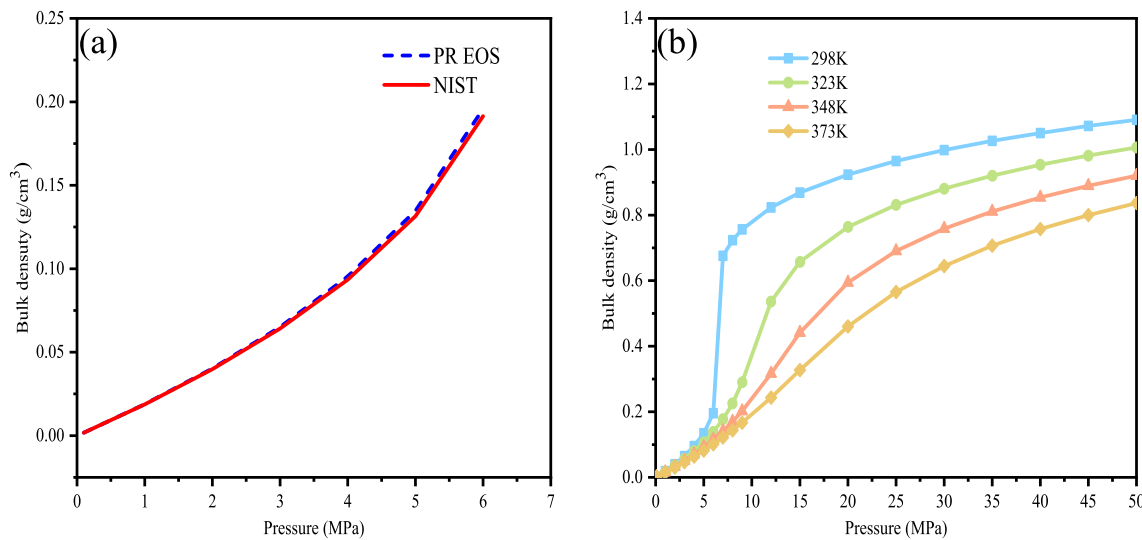


**Fig. 2.** (a) The bulk densities of  $\text{CO}_2$  obtained by PR equation and NIST database and (b) the bulk densities of  $\text{CO}_2$  from 298 K to 373 K with the increase of pressure.

which is widely used in clay minerals [54]. The potential model for  $\text{CO}_2$  was determined by three-site EPM2 model [55]. For water molecules, a SPC/E model developed from the simple point charge model (SPC) in CLAYFF force field was used [56]. For the bond and angle parameters in  $\text{CO}_2$  and water molecules, the C-O and H-O bond lengths are 1.162 Å and 1.0 Å, respectively. The angles of O-C-O and H-O-H are  $180^\circ$  and  $109.47^\circ$ , respectively. The nonbonded interactions between particles are described by Lennard-Jones (LJ)12–6 and coulomb terms [57], shown as:

$$E(r_{ij}) = 4\epsilon_{ij} \left[ \left( \frac{\sigma_{ij}}{r_{ij}} \right)^{12} - \left( \frac{\sigma_{ij}}{r_{ij}} \right)^6 \right] + \frac{q_i q_j}{4\pi\epsilon_0 r_{ij}} \quad (2)$$

$$\sigma_{ij} = \frac{1}{2} (\sigma_{ii} + \sigma_{jj}) \quad (3)$$

$$\epsilon_{ij} = \sqrt{\epsilon_i + \epsilon_j} \quad (4)$$

where  $r_{ij}$  represents the distance between the atom  $i$  and  $j$ .  $\epsilon_0$  is the dielectric constant with a value of  $8.85419 \times 10^{-12} \text{ F/m}$ .  $\epsilon_{ij}$  and  $\sigma_{ij}$  are the energy and distance parameters, respectively.  $q_i$  and  $q_j$  are the charges of atoms  $i$  and  $j$ . The parameters of  $\epsilon_{ij}$  and  $\sigma_{ij}$  for different atoms can be obtained by the Lorentz-Berthelot mixing rules in Eqs. (3) and (4) [58]. The nonbonded potential parameters of pyrophyllite,  $\text{CO}_2$  and water molecules were listed in Table S2.

### 2.3. Simulation details

All GCMC and MD simulations were performed by LAMMPS package [59]. Three-dimeson period boundary conditions and verlet algorithm with a timestep of 1.0 fs were applied in simulations [60]. The Nose-Hoover thermostat was used to keep the system temperature [61]. Considering the temperature and pressure conditions under different geological depths, the temperature in the simulations ranges from 298 K to 373 K, and the pressure from 0.1 MPa to 50 MPa. To investigate the effect of water content, simulations were carried out under nine different water contents. Water molecules were inserted into empty pyrophyllite nanopores to obtain pre-adsorbed water configurations. In GCMC simulation, the chemical potential ( $\mu$ ), box volume ( $V$ ), and temperature ( $T$ ) were fixed, and the gas pressure ( $P$ ) and fugacity coefficient ( $\phi$ ) instead of chemical potential were used in simulations. The fugacity coefficients obtained from Peng-Robinson (PR) equation of state [62]. The details of the calculation were shown in Eqs. S1-S7. The cutoff for van der Waals force and coulomb force were set to 1.2

nm and the long-range electrostatic interaction was calculated by Ewald summation method with a tolerance of  $1 \times 10^{-4}$  [63]. Each GCMC run consists of  $5 \times 10^6$  steps, the first 3 ns was for equilibrium and the last 2 ns was employed to obtain gas loading and energy information. The output equilibrium structure in GCMC simulation was used as input structure in MD simulation. For each molecular dynamic simulation, the cutoff was kept to 1.2 nm, and  $NVT$  ensemble was adopted. The first 1 ns was used to equilibrate the system and the last 2 ns was employed to obtain the trajectory information for analyzing.

## 3. Results and discussion

### 3.1. Bulk density

The bulk densities fitted from PR equation of state are compared with the NIST database [64]. The fitting results are similar to those of NIST in Fig. 2a. Based on this, the bulk phase density results in the simulations are shown in Fig. 2b. The critical constants of  $\text{CO}_2$  are 7.38 MPa ( $p_c$ ) and 304.2 K ( $T_c$ ) [65]. As the temperature increases, the gas density decreases accordingly. Under the condition that the temperature of  $\text{CO}_2$  is below 304.2 K, the bulk phase density rises slowly with the increase of pressure under low pressure (0–6 MPa), and rises sharply when the pressure is larger than 6 MPa, increasing from 4.43 mmol/g at 6 MPa to 15.37 mmol/g at 7 MPa. When the temperature is higher than the critical value, the bulk density of  $\text{CO}_2$  increases slowly with increasing pressure.

### 3.2. Adsorption capacity of $\text{CO}_2$ without water content

#### 3.2.1. Total and excess adsorption amount

The total and excess adsorption of  $\text{CO}_2$  are calculated in GCMC simulations. The total adsorption ( $n_t$ , mmol/g) is the amount of adsorbate loading in slit pores. The excess adsorption amount is defined in Eq. (5) [66]:

$$n_{ex} = n_t - \rho_{bulk} V_p \quad (5)$$

where  $\rho_{bulk}$  (mmol/ $\text{cm}^3$ ) is the bulk density obtained by PR equation of state and  $V_p$  ( $\text{cm}^3/\text{g}$ ) represents the pore volume between two clay sheets.  $V_p$  is obtained by zeo++ software, and the pore volume is measured by  $\text{CO}_2$  molecule which is used as molecular probe [67]. The simplified schematic diagram of gas adsorption is shown in Fig. S1. In addition to the total adsorption amount, the excess adsorption amount has the following relationship with the absolute adsorption amount

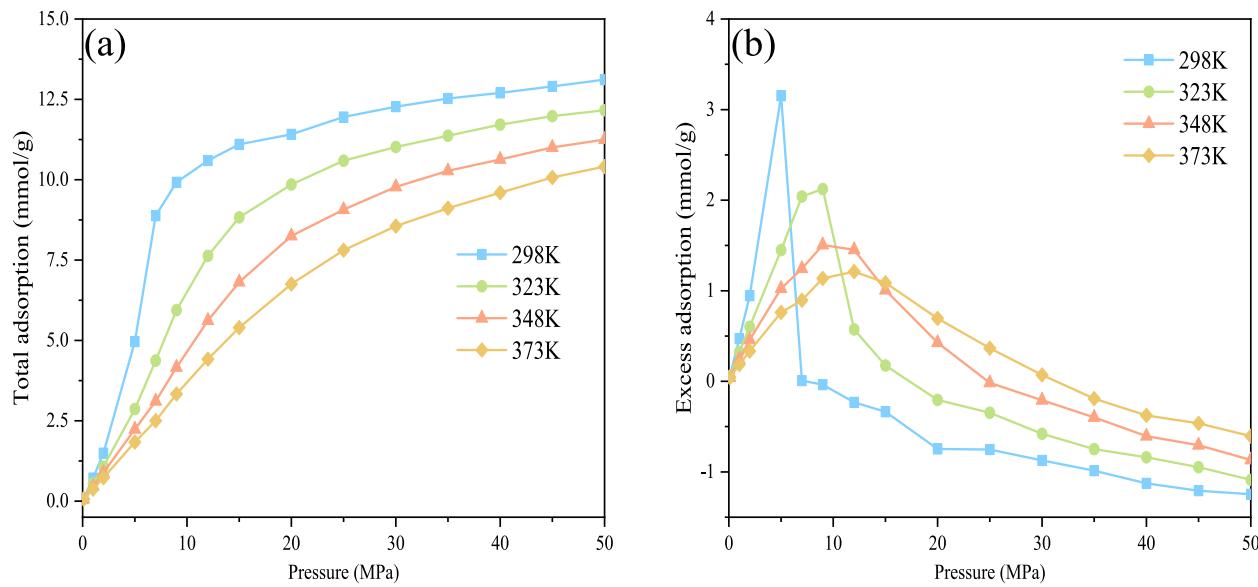


**Fig. 3.** The adsorption isotherm of CO<sub>2</sub>: (a) Total adsorption and (b) Excess adsorption.

**Table 1**  
Adsorbed phase density ( $\rho_{ads}$ ) of different methods.

Methods	Parameters	Temperature			
		298 K	323 K	348 K	373 K
Intercept method	$\rho_{ads}$	0.8691	0.8085	0.7808	0.7284
Modified Langmuir equation	$n_L$	4.9352	4.8434	4.2153	3.8017
	$p_L$	4.8035	8.0493	14.0875	18.1190
	$\rho_{ads}$	0.8849	0.8357	0.7935	0.7467
	$R^2$	0.8951	0.9387	0.9788	0.982
Empirical equation	$\rho_{ads}$	0.9869	0.9271	0.8709	0.8182

[68]:

$$n_{ex} = n_{abs} \left( 1 - \frac{\rho_{bulk}}{\rho_{ads}} \right) \quad (6)$$

where  $n_{abs}$  represents the absolute adsorption amount and  $\rho_{ads}$  represents the adsorption phase density. When the bulk phase density is larger than the adsorption phase density, the excess adsorption amount is lower than zero. Fig. 3 shows the total adsorption amount and excess adsorption amount varying with temperature and pressure. Total adsorption amount decreases with increasing temperature (Fig. 3a). In the process of GCMC adsorption simulations under low pressure, the excess adsorption amount increases rapidly (Fig. 3b). With the increase of pressure at 298 K, an inflection point appears in the isotherm adsorption curve at 5 ~ 7 MPa, and then the excess adsorption amount decreases. The excess adsorption amount increases to a maximum value

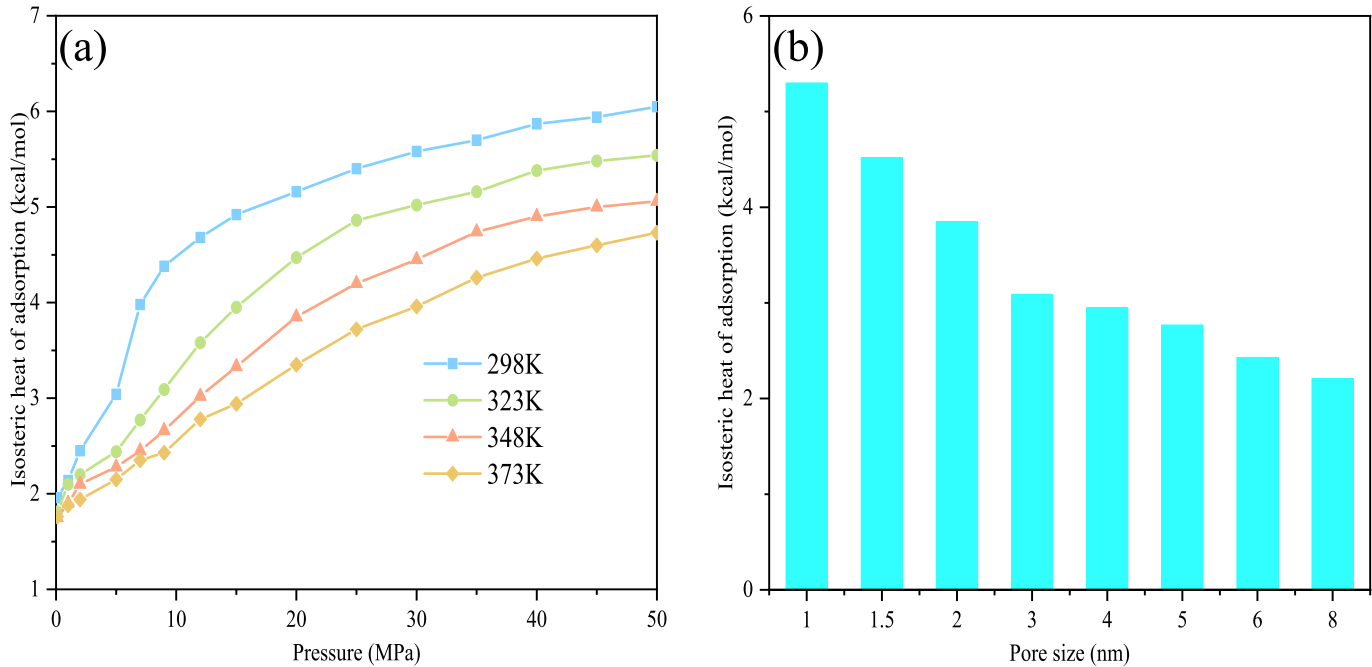


**Fig. 4.** Isosteric heat of adsorption (a) from 298 K to 373 K with the increase of pressure,  $h = 3$  nm, and (b) with the pore size from 1 nm to 8 nm at 323 K and 9 MPa.

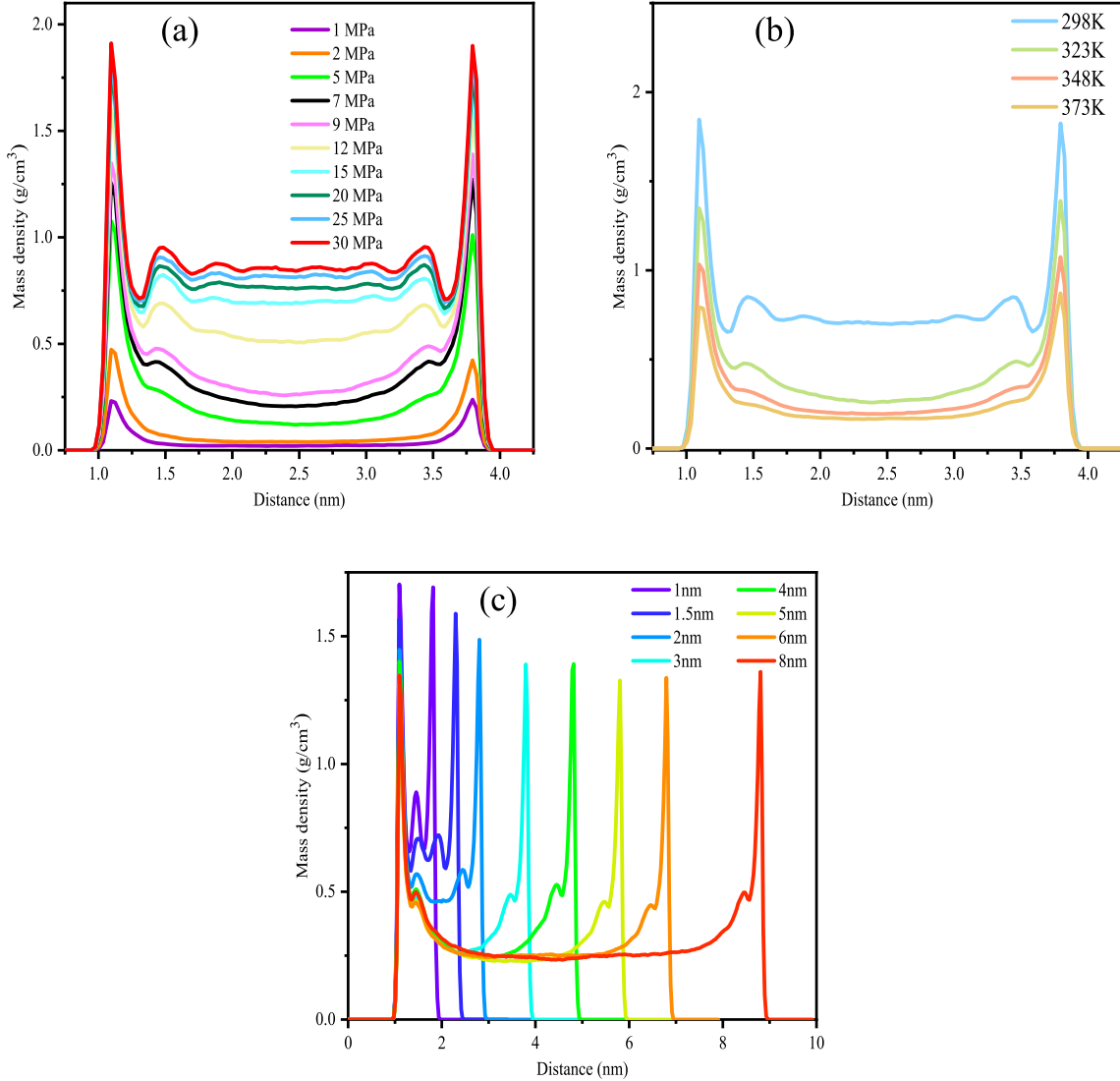


**Fig. 5.** Mass density profiles of  $\text{CO}_2$  (a) at 323 K varying with pressure,  $h = 3 \text{ nm}$ ; (b) at 9 MPa varying with temperature,  $h = 3 \text{ nm}$ ; and (c) at 323 K and 9 MPa varying with pore size.

and then declines as the pressure increases. Under low pressure (less than 5 MPa), the excess adsorption amount decreases with the increase of temperature. The pressure corresponding to the maximum excess adsorption amount increases as the temperature increases. After the maximum excess adsorption amount is exceeded, the lower the temperature, the faster the curve decreases. When pressure is larger than 15 MPa, excess adsorption amount increases with the increase of temperature. It can be explained that the density of the bulk phase at low temperatures becomes larger with the pressure rising.

### 3.2.2. Adsorption phase density

In order to better describe excess adsorption amount, it is necessary to determine the density of adsorption phase. There are many methods to determine the density of adsorbed phase, and one empirical equation is:

$$\rho_{ads} = \rho_b \exp(-0.0025 \times (T - T_b)) \quad (7)$$

where  $\rho_b$  is the density and  $T_b$  is the temperature of boiling at the boiling point of  $\text{CO}_2$  at atmospheric pressure [69].  $\rho_b$  and  $T_b$  are assumed to be  $1277.78 \text{ kg/m}^3$  and  $194.67 \text{ K}$ , respectively. Another widely used method (Intercept method) is using the pressure corresponding to the intersection of excess adsorption curve with x-axis, and

density of adsorbed phase ( $\rho_{ads}$ ) is equal to the bulk density calculated from PR EOS under this pressure. In the experiment, researchers employed the Langmuir equation to fit the density of adsorbed phase at the corresponding temperature [70–73]. Typically, the Langmuir equation was described as followed in Eq. (8):

$$n_{abs}(T) = n_L \frac{P}{P + P_L(T)} \quad (8)$$

where  $n_{abs}$  is the absolute adsorption amount at a temperature  $T$ ,  $n_L$  is the maximum adsorption capacity of Langmuir, and  $P_L$  is Langmuir pressure. However, this model is only applicable for monolayer adsorption. For multilayer adsorption, the Langmuir equation was improved to better apply it to the adsorption behavior of supercritical fluids [74]. The modified Langmuir equation expression is as follow:

$$n_{ex} = n_L \left( \frac{P}{P + P_L} \right) \left( 1 - \frac{\rho_{bulk}}{\rho_{ads}} \right) \quad (9)$$

where  $n_L$  is the max Langmuir adsorption,  $P_L$  is the Langmuir pressure when the adsorption capacity reaches the maximum adsorption amount. The fitting results of adsorption isotherm model are shown in Table 1. It can be seen that the density of adsorbed phase decreases with increase of temperature, because the possibility of  $\text{CO}_2$  desorbing from adsorbed

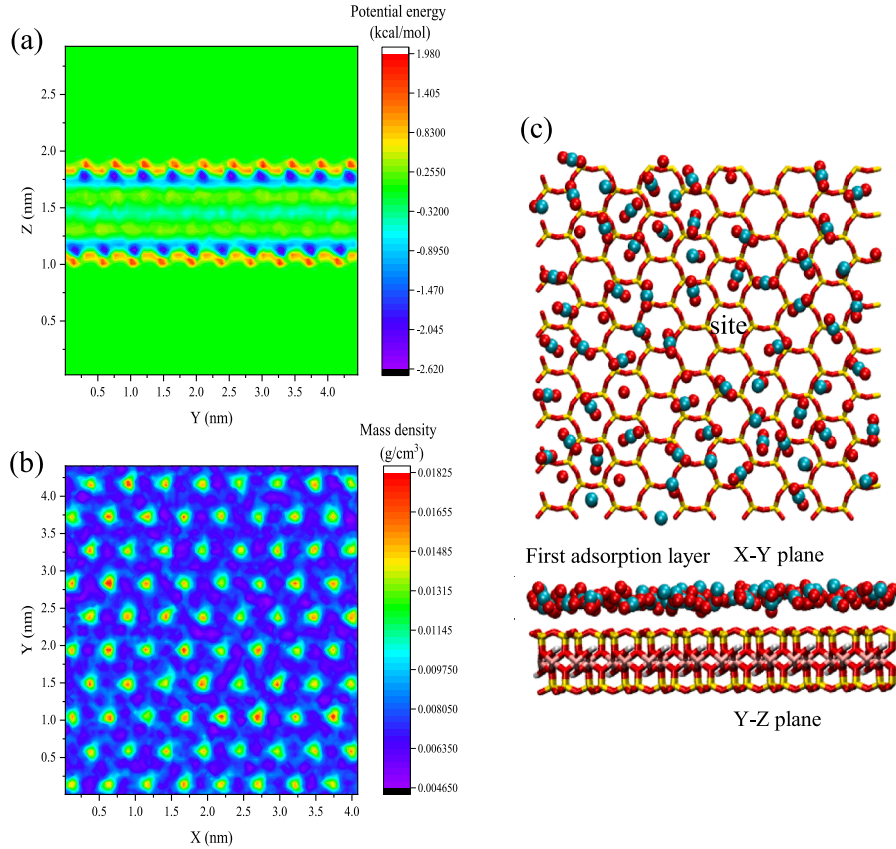


**Fig. 6.** Two-dimensional (2d) (a) potential energy distribution (Y-Z plane) at 323 K and 9 MPa,  $h = 1 \text{ nm}$ ; (b) mass density distribution of  $\text{CO}_2$  (X-Y plane) of the first adsorption layer; and (c) snapshots of  $\text{CO}_2$  in first adsorption layer (X-Y plane and Y-Z plane). “site” in six-membered ring represents the location of the adsorption sites.

phase to free phase increases as the temperature rises, leading to the reduction of  $\text{CO}_2$  adsorption amount. Comparing with Langmuir equation and its improved model, density of adsorbed phase obtained by the intercept method is smaller. Under the conditions of  $0 \sim 50 \text{ MPa}$ ,  $298 \sim 423 \text{ K}$ , the density range of  $\text{CO}_2$  adsorbed on the illite surface was from  $0.997$  to  $0.803 \text{ g}/\text{cm}^3$  [36]. Obviously, the density of adsorbed phase calculated by empirical equation is larger than that by the other methods in Table 1, and the value obtained by the improved Langmuir equation and Intercept method is smaller than that obtained by the illite model simulation. It can be explained that the adsorption capacity of illite is stronger than that of pyrophyllite because of its hydrophilicity and metal cations in slit pores. Previous molecular dynamics simulation studies have demonstrated that hydrophilic minerals with interlayer cations have strong adsorption capacity. Cations existed in interlayer of clay minerals due to element replacement have strong interaction with  $\text{CO}_2$  [75]. In addition, it can be noted that the improved Langmuir equation has better fitting effect at high temperature as presented in Table 1. From the result of equation fitting, the Langmuir adsorption amount of  $\text{CO}_2$  decreases from  $4.9352 \text{ mmol/g}$  at  $298 \text{ K}$  to  $3.8017 \text{ mmol/g}$  at  $373 \text{ K}$ . In contrast, Langmuir pressure increases from  $4.8305 \text{ MPa}$  at  $298 \text{ K}$  to  $18.1190 \text{ MPa}$  at  $373 \text{ K}$ .

The density distribution curve in Fig. 5a shows that the density of the adsorbed phase depends on the pressure. Even at high pressure, the density of the adsorbed phase increases with increasing pressure but not reaching a plateau. The above three calculation methods in Table 1 ignore the influence of pressure. In molecular simulation, the absolute adsorption amount and the adsorbed phase volume can be obtained by density distribution curve as shown in Fig. S2. The adsorbed phase density at 323 K is calculated and shown in Fig. S3. Compared with other methods, the results obtained from adsorbed phase can well characterize

the trend of the excess adsorption isotherm.

### 3.2.3. Isosteric heat of adsorption

Isosteric heat of adsorption is an important thermodynamic parameter to characterize the strength of gas adsorption, the formula for calculating the heat of adsorption in this work is given by Eq. (10):

$$Q_{st} = k_B T - \frac{\langle UN \rangle - \langle U \rangle \langle N \rangle}{\langle N^2 \rangle - \langle N \rangle^2} \quad (10)$$

where  $k_B$  is the Boltzmann constant,  $T$  is temperature,  $U$  is total potential energy of the system, and  $N$  is the uptake number of gas molecules [76,77]. The bracket indicates the ensemble average.

Fig. 4 shows the isosteric heat of adsorption at different temperatures, pressures, and pore apertures. At constant temperature, the adsorption heat released through  $\text{CO}_2$  adsorption on the pyrophyllite increases with increasing pressure mainly originating from the increased interaction among  $\text{CO}_2$  molecules under high pressure [78,79]. Whereas with the increase in temperature, the strength of adsorption decreases. This indicates that the interaction between adsorbent and adsorbate molecules decreases with the increase in temperature. The isosteric adsorption heat decreases rapidly because of the overlapping effect with the slit pore size increasing from  $1 \text{ nm}$  to  $3 \text{ nm}$ . The overlapping effect is the surface attraction overlapping in narrow pores [80]. The range of slit pore size influenced by overlapping effect is larger than that of some previous studies because  $\text{CO}_2$  was more easily adsorbed on the surface of clay minerals than  $\text{CH}_4$  [81]. Since the equivalent adsorption heat of physical adsorption was less than  $40 \text{ kJ/mol}$  (about  $9.6 \text{ kcal/mol}$ ), the adsorption of  $\text{CO}_2$  on the pyrophyllite surface was physical adsorption [82]. With the increase of temperature, the isosteric heat of adsorption decreases, leading to the change of adsorbate from the adsorption phase

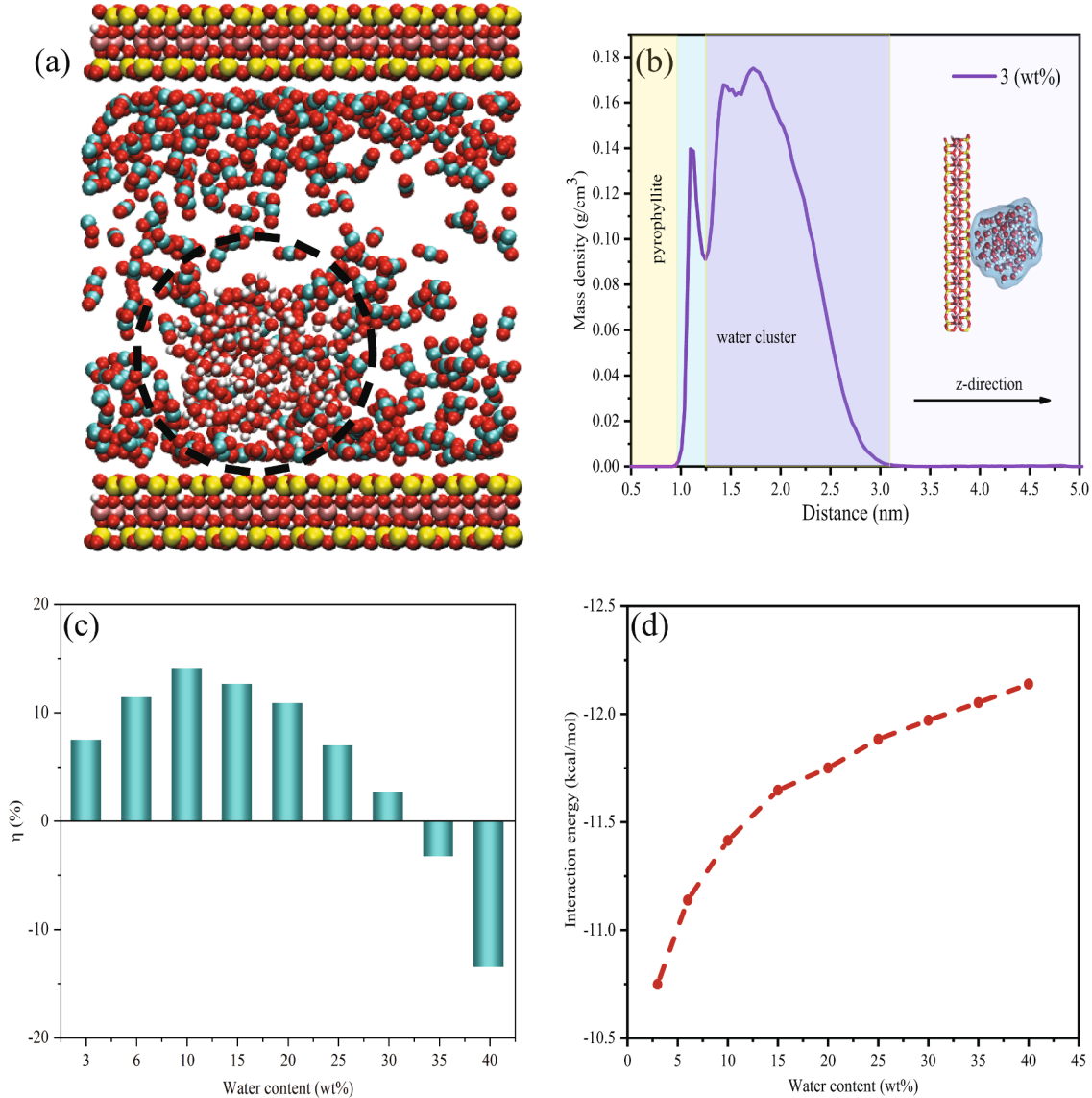


**Fig. 7.** (a) A snapshot of adsorption configuration with 3 wt% water content; (b) mass density profile of water along z-axis; (c) the storage reduction efficiency  $\eta$  varying with water content; (d) the interaction energy per water molecule within water clusters.

to the free phase and the decrease of absolute adsorption amount [83].

#### 3.2.4. Density profile

The pore size and pressure effect of  $\text{CO}_2$  distribution in slit pores are shown in Fig. 5. With the increase in pressure, the adsorption phase changes from a monolayer to a double layer (a strong adsorption layer and a weak adsorption layer). As the pressure is less than 7 MPa which is similar to the critical pressure of  $\text{CO}_2$  (7.38 MPa), the first adsorption layer is formed. When the pressure is larger than 7 MPa, an extra weak (second) adsorption layer forms. The peak value of adsorbed phase density becomes higher as the pressure increases (Fig. 5a). However, higher temperature will lead to the reduction of the first adsorption peak (Fig. 5b). When the pore size is larger than 3 nm, the peak value is similar in both the first and second adsorption layers (Fig. 5c). The increase in temperature leads to the weakening of adsorption, and higher pressure is required to form a second adsorption layer at high temperatures. At 9 MPa, the second adsorption layer at high temperatures (348 K and 373 K) almost disappears as performed in Fig. 5b. Therefore, the number of  $\text{CO}_2$  adsorption layers in the pyrophyllite pores and the peak density near the pore wall are affected by temperature, pressure, and

pore aperture.

#### 3.2.5. Adsorption sites

According to the above discussion, because of the overlapping effect, smaller slit pores and lower temperatures contribute to the higher density of  $\text{CO}_2$  on the clay surface. To determine the adsorption sites of gases on the pore wall, two two-dimensional maps of potential energy and gas mass density within a pore size of 1 nm at 298 K are selected. As shown in Fig. 6a, the blue area represents the molecular potential energy as an attraction in the y-z plane which corresponds to the position of first adsorption layer (1.1 ~ 1.2 nm). The green area in Fig. 6b represents the concentration center of  $\text{CO}_2$ . Combined with the mass density profile of gas in the x-y plane, the adsorption site is mainly located in the center of a six-membered ring composed of six silicon oxide tetrahedrons. The snapshot of  $\text{CO}_2$  in the first adsorption layer is shown in Fig. 6c.

#### 3.3. Effect of water content on adsorption

Nine different water contents (between 3 wt% and 40 wt%) are used to study the impact of  $\text{CO}_2$  adsorption at 323 K and 9 MPa. The snapshots

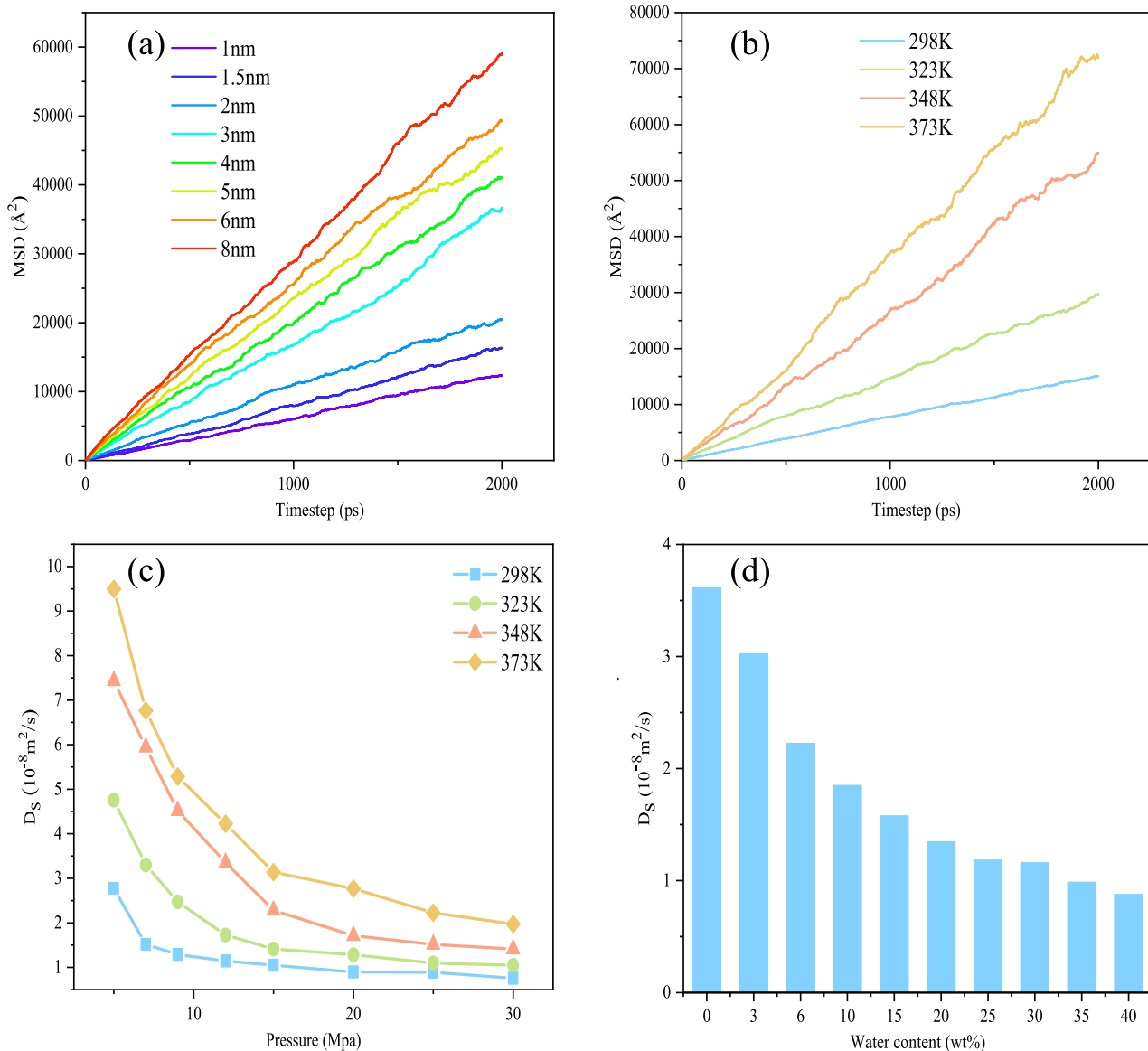


**Fig. 8.** (a) The MSD curves of different pore sizes at 323 K and 9 MPa; (b) the MSD curves of different temperatures,  $h = 3$  nm; (c) the self-diffusion coefficients of different pressures at 323 K,  $h = 3$  nm; (d) the self-diffusion coefficients of different water contents at 323 K and 9 MPa.

of adsorption are shown in Fig. S4. The density distribution curves of water molecules with different water contents are shown in Fig. S5. As the water content increases, the water clusters in the pores gradually move away from the mineral surface (see Fig. S4). At low water content, water molecules tend to form droplet due to surface tension (Fig. 7a). Although the surface of pyrophyllite is hydrophobic, a small part of water molecules (water content below 25 wt%) is still adsorbed on the clay surface (Fig. S5). The binding energy between water and pyrophyllite induce a weak adsorption layer located between 1 ~ 1.25 nm along the z-axis direction which is in good agreement with the previous study [84]. Fig. 7b shows the mass distribution of water molecules along the z-axis when water content is 3 wt%. To evaluate the effect of water content on  $\text{CO}_2$  adsorption, the storage reduction efficiency  $\eta$  is used to provide the insight in  $\text{CO}_2$  adsorption as given in Eq. (11) [43]:

$$\eta = \frac{\langle N_{\text{wt}\%=i} \rangle - \langle N_{\text{wt}\%=0} \rangle}{\langle N_{\text{wt}\%=0} \rangle} \times 100\% \quad (11)$$

where  $\langle N_{\text{wt}\%=i} \rangle$  and  $\langle N_{\text{wt}\%=0} \rangle$  represent the ensemble-averaged number of  $\text{CO}_2$  in slit pores with different water content  $i$  and in the absence of water ( $i=0$ ). Positive and negative values indicate an increase and

decrease in  $\text{CO}_2$  adsorption amount. The results in Fig. 7c show that the storage reduction efficiency  $\eta$  first increases and then decreases with increasing water content, reaching a maximum value at the water content of 10 wt%. However, it is negative when the water contents are 35 wt% and 40 wt%. Overall, when the water content is below 30 wt%, the presence of water has an enhancing effect on  $\text{CO}_2$  adsorption, while it has a weakening effect when water content reaches 35 wt%. Fig. 7d reveals the interaction energy per water molecule within water clusters in the presence of different water contents. The interaction energy consists of Coulombic energy and van der Waals interaction energy. With the increase of water content, the interaction energy between water molecules increases. Meanwhile, the pore volume for storing  $\text{CO}_2$  molecules decreases as the water content increases (Fig. S4). On the other hand, previous research showed that in hydrophilic minerals such as montmorillonite and kerogen, the adsorption capacity of gas decreased with the increase of water content [39]. For hydrophilic minerals, with the increase of water content, water molecules and adsorbates are adsorbed competitively on the mineral surface, and some adsorption sites are occupied by water molecules, leading to the decrease of gas adsorption amount.

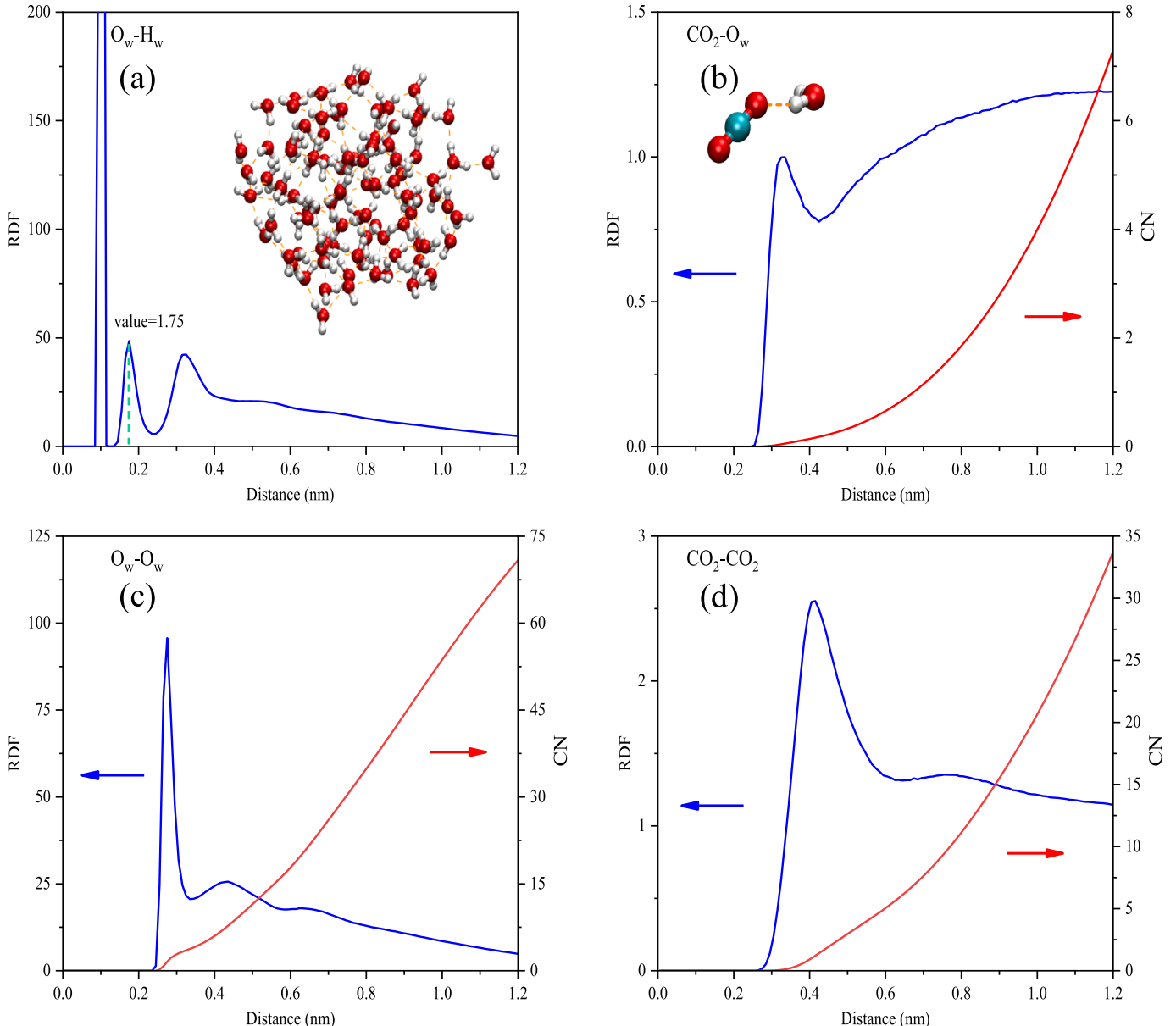


**Fig. 9.** Radial distribution function (blue line) and coordination number (red line) curves of different atoms in CO<sub>2</sub> and water molecules. (a) O<sub>w</sub>-H<sub>w</sub>; (b) CO<sub>2</sub>-O<sub>w</sub>; (c) O<sub>w</sub>-O<sub>w</sub>; (d) CO<sub>2</sub>-CO<sub>2</sub>.

#### 3.4. Dynamic characteristics of interlayer molecules

##### 3.4.1. Diffusion properties of molecules

Mean square displacement (MSD) represents the diffusion properties of matter that are calculated with the last 2 ns in MD simulation. Self-diffusion coefficient ( $D_s$ ) is calculated from Einstein equation described by Eq. (12) [85]:

$$D_s = \frac{1}{6N} \lim_{t \rightarrow \infty} \frac{d}{dt} \sum_{i=1}^N [r_i(t) - r_i(0)]^2 \quad (12)$$

where  $r_i(t)$  and  $r_i(0)$  represent the position of  $i$  th atom at time  $t$  and initial time, and  $N$  is the uptake number of gas molecules every 1000 steps.

The MSD curve in Fig. 8a shows the influence of pore aperture on CO<sub>2</sub> diffusion. The results reveal that the upward trend of diffusion in a larger slit pore which causes a higher self-diffusion coefficient. The increasing space for molecular motion in larger slit pores can be

explained by this trend. Fig. 8b shows the MSD curve of CO<sub>2</sub> from 298 K to 373 K. According to the simulation results, the slope of MSD curve increases with the increase of temperature. It can be explained by the higher kinetic energy of gas molecules at high temperatures. Fig. 8c shows the self-diffusion coefficients of CO<sub>2</sub> under four temperatures with pressure varying from 5 MPa to 30 MPa. For the pressure from 5 MPa to 15 MPa, an obvious downward trend could be observed. The turning points of the curve changing from 7 MPa at 298 K and 15 MPa at 373 K indicate the decrease of sensitivity of CO<sub>2</sub> bulk density to pressure change at high temperatures (Fig. 2b). When pressure exceeds 20 MPa, the self-diffusion coefficient is less affected by the pressure. The self-diffusion coefficient is shown in Fig. 8d, the increase of water content can reduce the diffusion capacity of CO<sub>2</sub>. In contrast, in hydrophilic clay minerals such as montmorillonite, the diffusion capacity of gases enhances with the increase of water content [86]. For hydrophilic clay minerals, with the increase of water content, more adsorption sites on the clay surface are occupied by water. Generally, some adsorbate will gradually release from adsorbed phase into the free phase due to the

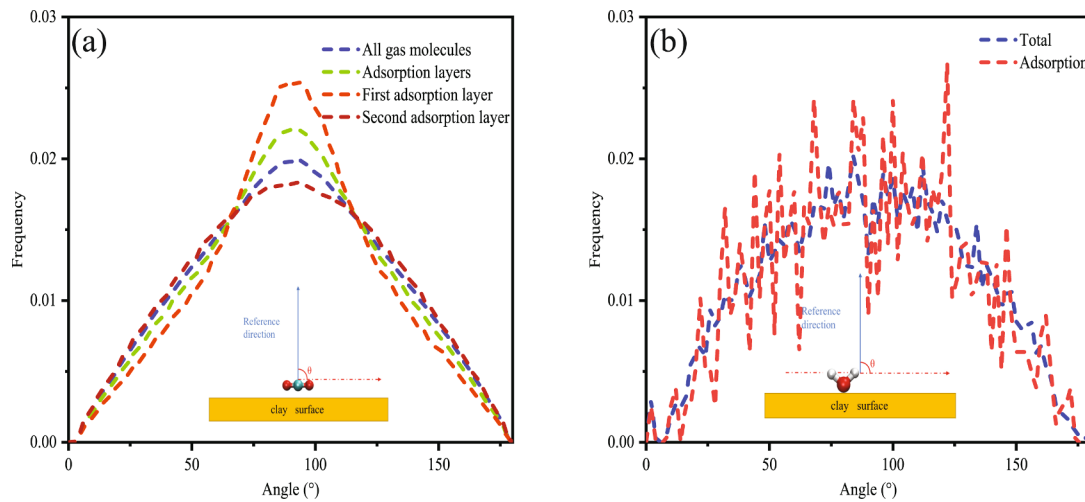


**Fig. 10.** The frequency distribution of inclination angle and its definition of (a)  $\text{CO}_2$  and (b) water.

reduction of adsorption sites. Because of the hydrophobicity of pyrophyllite, water molecules occupy fewer adsorption sites on clay surface, and a large number of sites are occupied by  $\text{CO}_2$  molecules. In addition, with the increase of interlayer water content, the effective pore volume decreases, and the diffusion ability of  $\text{CO}_2$  molecules decreases because of the smaller space.

#### 3.4.2. Radial distribution functions of small molecules

In order to further study the distribution characteristics of water and carbon dioxide in pyrophyllite with moisture. The radial distribution functions (RDFs) of  $\text{O}_w$  (water oxygen) around  $\text{CO}_2$ ,  $\text{O}_w\text{-H}_w$  (oxygen and hydrogen atoms of water molecules),  $\text{CO}_2\text{-CO}_2$  and  $\text{O}_w\text{-O}_w$  are calculated with a cut-off radius of 1.2 nm. As shown in Fig. 9a, the first peak of  $\text{H}_w\text{-O}_w$  at 0.1 nm represents the distance between the oxygen and the hydrogen atom in water molecules, which is consistent with the bond distance. Then, a second peak located at 1.7 Å is similar to the results of AIMD simulations (1.68 Å) [49]. According to the definition, the distance between hydrogen and oxygen atoms in forming strong hydrogen bonds was between 1.5 ~ 2.2 Å [87], which covers the location of the second peak in Fig. 9a. To further investigate the interaction relationship between water molecules as water content increases, the average hydrogen bonds per water molecule within water clusters ( $n_{HB}$ ) are calculated. The geometrical criterion is from Luzar and Chandler, in which a hydrogen bond is determined with a length of  $\text{O}\cdots\text{H}$  less than 3.5 Å and an angle of  $\angle\text{O}\cdots\text{O}\cdots\text{H}$  smaller than  $30^\circ$  [88]. Fig. S6 indicates the enhancement of interaction between water molecules as the water content increase, corresponding to the results in Fig. 7d. Fig. 9b shows the RDF and coordination number (CN) of  $\text{CO}_2\text{-O}_w$ . A peak at a distance of 3.3 Å with low CN indicates that some  $\text{CO}_2$  molecules are hydrated during the adsorption process because of the interaction between  $\text{CO}_2$  and water. As shown in Fig. 9c and Fig. 9d, the RDF distribution curve of  $\text{CO}_2$  molecule and water oxygen are given. A peak value of the  $\text{O}_w\text{-O}_w$  RDF located at about 2.7 Å is also in the range of the distance (2.5–3.2 Å) between the donor and recipient atoms of the strong hydrogen bond. Because of the intermolecular force of  $\text{CO}_2$ , there is a peak value at around 0.4 nm in  $\text{CO}_2\text{-CO}_2$  RDF, similar to some previous simulations [36].

#### 3.4.3. Angle distribution of $\text{CO}_2$ and water

In slit pores of clay minerals, the adsorbate is in a confined state, and molecules will have a specific spatial inclination angle due to the adsorption of pore wall surface and interaction between molecules. Fig. 10a shows the inclination angle distribution of  $\text{CO}_2$  at 323 K and 9 MPa. Fig. 10b shows the inclination angle distribution of water molecules between pyrophyllite layers with 3 wt% water content at 323 K

and 9 MPa. The adsorption inclination angle is defined as the angle between the adsorbate molecule and the adsorbent surface in the vertical direction. For  $\text{CO}_2$  molecules, the inclination angle is defined as the angle between in line with three atoms of  $\text{CO}_2$  and the normal direction of the clay mineral surface [15]. For water molecules, it is the angle between the connecting line of two hydrogen atoms and the normal direction of the clay mineral surface [89]. The inclination angle distribution of all molecules of  $\text{CO}_2$  in the pore and adsorption layer (including the first adsorption layer and second adsorption layer) is calculated. As a result, the inclination angle of  $\text{CO}_2$  in the adsorption layer is mainly distributed at an angle of  $90^\circ$ , indicating that  $\text{CO}_2$  molecules are mainly adsorbed on the surface of pyrophyllite in parallel. Compared with the second adsorption layer, the inclination angle of the first adsorption layer is more concentrated at  $90^\circ$  with a larger frequency of about 0.025. On the other hand, it can be seen that the inclination angle of water molecules in the interlayer or weak adsorption layer is widely distributed without obvious directivity. Similarly, the molecular orientation distribution could be found at the hydrophobic talc-water interface [89].

## 4. Conclusion

In this study, the adsorption and diffusion behavior of  $\text{CO}_2$  in pyrophyllite slit pores were studied in detail by combining GCMC and MD simulation. The influence of several factors such as pore aperture, temperature, pressure, and water content were taken into account. The excess adsorption amount of  $\text{CO}_2$  initially increases to a maximum value and then decreases as the pressure rises. The variation trend of the excess adsorption amount is related to the density of bulk phase and adsorbed phase densities. For pore apertures smaller than 3 nm, the peak value of mass density will increase as the pore aperture decreases owing to the overlapping effect. Compared with the large pore aperture of pyrophyllite, the adsorption heat of the small ones is higher, and the gas diffusion capacity is lower. When the water content is less than 30 wt%, water enhances the adsorption of  $\text{CO}_2$ . Conversely, when the water content exceeds 35 wt%, it reduces the amount of  $\text{CO}_2$  adsorption. On the other hand, the self-diffusion coefficient of  $\text{CO}_2$  decreases as water content increases. The adsorption behavior of  $\text{CO}_2$  on the pyrophyllite surface has a significant orientation, mainly in a parallel configuration.

In underground aquifers, the adsorption and flow behavior of  $\text{CO}_2$  in nanopores are closely related to water. Due to the diversity of mineral types and the presence of mixed-layer minerals, water can occur in various forms within mineral pores. The clusters of water in hydrophobic nanopores and the water film formed by hydrophilic nanopores jointly affect the flow and adsorption behavior of  $\text{CO}_2$ . The formation of

water clusters in siloxane nanopores can effectively hinder the migration of CO<sub>2</sub> fluid, while the water film in gibbsite pores reduces CO<sub>2</sub> adsorption by covering the mineral surface [90,91]. Furthermore, in nanopores composed of hydrophilic and hydrophobic surfaces, such as kaolinite, the occurrence form of water can become more complex under different water contents. Our analysis of water content in pyrophyllite slit pores reveals that the presence of water not only increases the adsorption amount of CO<sub>2</sub> but also hinders its diffusion ability. Our results can provide essential insights for further studies of the flow behavior of CO<sub>2</sub> in mineral pores composed of hydrophobic surfaces under different temperature and pressure conditions at micro and nano scales. In addition, especially in salt water layers, fluids often contain various salt ions such as K<sup>+</sup>, Na<sup>+</sup>, Li<sup>+</sup>, Mg<sup>2+</sup>, and Ca<sup>2+</sup>. The interaction mechanism of hydrophobic clay-brine system should also be explored in future research.

### Declaration of Competing Interest

The authors declare that they have no known competing financial interests or personal relationships that could have appeared to influence the work reported in this paper.

### Data availability

Data will be made available on request.

### Acknowledgments

This study was supported by the National Natural Science Foundation of China (42273036, 41902133) and Guangzhou Science and Technology Planning Project (202102020943). The calculations were performed at the National Supercomputer Center in Guangzhou. We thank the three anonymous reviewers for their constructive comments, and Qun Yi for his comments and efficient editorial handling.

### Appendix A. Supplementary data

Supplementary data to this article can be found online at <https://doi.org/10.1016/j.fuel.2023.128917>.

### References

- [1] Altman SJ, Aminzadeh B, Balhoff MT, Bennett PC, Bryant SL, Cardenas MB, et al. Chemical and hydrodynamic mechanisms for long-term geological carbon storage. *J Phys Chem C* 2014;118(28):15103–13.
- [2] Bui M, Adjiman CS, Bardow A, Anthony EJ, Boston A, Brown S, et al. Carbon capture and storage (CCS): the way forward. *Energy Environ Sci* 2018;11(5):1062–176.
- [3] Haszeldine RS. Carbon capture and storage: how green can black be? *Science* 2009;325(5948):1647–52.
- [4] Bachu S. Sequestration of CO<sub>2</sub> in geological media: criteria and approach for site selection in response to climate change. *Energy Convers Manage* 2000;41(9):953–70.
- [5] Bickle MJ. Geological carbon storage. *Nature Geosci* 2009;2(12):815–8.
- [6] Orr FM. Onshore geologic storage of CO<sub>2</sub>. *Science* 2009;325(5948):1656–8.
- [7] Ma Z, Ranjith PG. Review of application of molecular dynamics simulations in geological sequestration of carbon dioxide. *Fuel* 2019;255:115644.
- [8] Aminu MD, Nabavi SA, Rochele CA, Manovic V. A review of developments in carbon dioxide storage. *Appl Energy* 2017;208:1389–419.
- [9] Shi Q, Cui S, Wang S, Mi Y, Sun Q, Wang S, et al. Experiment study on CO<sub>2</sub> adsorption performance of thermal treated coal: Inspiration for CO<sub>2</sub> storage after underground coal thermal treatment. *Energy* 2022;254:124392.
- [10] Chen G, Lu S, Liu K, Han T, Xu C, Xue Q, et al. GCMC simulations on the adsorption mechanisms of CH<sub>4</sub> and CO<sub>2</sub> in K-illite and their implications for shale gas exploration and development. *Fuel* 2018;224:521–8.
- [11] Ma Y, Lu G, Shao C, Li X. Molecular dynamics simulation of hydrocarbon molecule adsorption on kaolinite (0 0 1) surface. *Fuel* 2019;237:989–1002.
- [12] Hinkov I, Lamari F, Langlois P, Dicko M, Chiley C, Pentchev I. Carbon dioxide capture by adsorption. *J Chem Technol Metall* 2016;51(6):609–26.
- [13] Awad AM, Shaikh SMR, Jalab R, Gulied MH, Nasser MS, Benamor A, et al. Adsorption of organic pollutants by natural and modified clays: a comprehensive review. *Sep Purif Technol* 2019;228:115719.
- [14] Tao H, Qian Xi, Zhou Yi, Cheng H. Research progress of clay minerals in carbon dioxide capture. *Renew Sustain Energy Rev* 2022;164:112536.
- [15] Myshakin EM, Saidi WA, Romanov VN, Cygan RT, Jordan KD. Molecular dynamics simulations of carbon dioxide intercalation in hydrated Na-montmorillonite. *J Phys Chem C* 2013;117(21):11028–39.
- [16] Mukhopadhyay TK, Ghatak S, Maiti HS. Pyrophyllite as raw material for ceramic applications in the perspective of its pyro-chemical properties. *Ceram Int* 2010;36(3):909–16.
- [17] Zhang L, Lu X, Liu X, Yang K, Zhou H. Surface wettability of basal surfaces of clay minerals: Insights from molecular dynamics simulation. *Energy Fuels* 2016;30(1):149–60.
- [18] Abedini A, Khosravi M, Mongelli G. The middle Permian pyrophyllite-rich ferruginous bauxite, northwestern Iran, Iran-Impalayan karst belt: Constraints on elemental fractionation and provenance. *J Geochem Explor* 2022;233:106905.
- [19] Bauluz B, Subías I. Coexistence of pyrophyllite, I-S, R1 and NH4+-rich illite in Silurian black shales (Sierra de Albaracín, NE Spain): metamorphic vs. hydrothermal origin. *Clay Miner* 2010;45(3):383–92.
- [20] Wu H, He M, Wu S, Yang M, Liu X. Near-Infrared Spectroscopy Study of OH Stretching Modes in Pyrophyllite and Talc. *Crystals* 2022;12(12):1759.
- [21] Hu Y, Liu X, Xu Z. Role of crystal structure in floatation separation of diaspore from kaolinite, pyrophyllite and illite. *Miner Eng* 2003;16(3):219–27.
- [22] Sinyakovskaya I, Zaykov V, Kitagawa R. Types of pyrophyllite deposits in foldbelts. *Resource Geol* 2005;55(4):405–18.
- [23] Greathouse JA, Cygan RT. Water Structure and Aqueous Uranyl(VI) Adsorption Equilibria onto External Surfaces of Beidellite, Montmorillonite, and Pyrophyllite: Results from Molecular Simulations. *Environ Sci Technol* 2006;40(12):3865–71.
- [24] Erdemoğlu M, Erdemoğlu S, Sayılık F, Akarsu M, Şener S, Sayılık H. Organofunctional modified pyrophyllite: preparation, characterisation and Pb(II) ion adsorption property. *Appl Clay Sci* 2004;27(1):41–52.
- [25] Gücek A, Şener S, Bilgen S, Mazmanci MA. Adsorption and kinetic studies of cationic and anionic dyes on pyrophyllite from aqueous solutions. *J Colloid Interface Sci* 2005;286(1):53–60.
- [26] Kerisit S, Okumura M, Rosso KM, Machida M. Molecular Simulation of Cesium Adsorption at the Basal Surface of Phyllosilicate Minerals. *Clays Clay Miner* 2016;64(4):389–400.
- [27] Sheng J, Xie Y, Zhou Y. Adsorption of methylene blue from aqueous solution on pyrophyllite. *Appl Clay Sci* 2009;46(4):422–4.
- [28] Zhang J, Zhou Y, Jiang M, Li J, Sheng J. Removal of methylene blue from aqueous solution by adsorption on pyrophyllite. *J Mol Liq* 2015;209:267–71.
- [29] Li W, Nan Y, Zhang Z, You Q, Jin Z. Hydrophilicity/hydrophobicity driven CO<sub>2</sub> solubility in kaolinite nanopores in relation to carbon sequestration. *Chem Eng J* 2020;398:125449.
- [30] Angelini MM, Garrard RJ, Rosen SJ, Hinrichs RZ. Heterogeneous Reactions of Gaseous HNO<sub>3</sub> and NO<sub>2</sub> on the Clay Minerals Kaolinite and Pyrophyllite. *J Phys Chem A* 2007;111(17):3326–35.
- [31] Shiga M, Morishita T, Aichi M, Sorai M. Effect of Surface Coverage of Water Molecules on Methane Adsorption on Muscovite and Pyrophyllite: Molecular Dynamics Study. *Energy Fuels* 2021;35(24):19986–99.
- [32] Bibi I, Icenhower J, Niazi NK, Naz T, Shahid M, Bashir S. Chapter 21 - Clay Minerals: Structure, Chemistry, and Significance in Contaminated Environments and Geological CO<sub>2</sub> Sequestration. In: Prasad MNV, Shih K, editors. Environmental Materials and Waste. Academic Press; 2016, p. 543–67.
- [33] Chouikhi N, Cecilia JA, Vilarrasa-García E, Besghaier S, Chlendi M, Franco Duro FI, et al. CO<sub>2</sub> Adsorption of Materials Synthesized from Clay Minerals: A Review. *Minerals* 2019;9(9):514.
- [34] Makaremi M, Jordan KD, Guthrie GD, Myshakin EM. Multiphase monte carlo and molecular dynamics simulations of water and CO<sub>2</sub> intercalation in montmorillonite and beidellite. *J Phys Chem C* 2015;119(27):15112–24.
- [35] Yang Y, Narayanan Nair AK, Sun S. Layer charge effects on adsorption and diffusion of water and ions in interlayers and on external surfaces of montmorillonite. *ACS Earth Space Chem* 2019;3(11):2635–45.
- [36] Zhang J, Cennell MB, Liu K, Pervukhina M, Chen G, Dewhurst DN. Methane and carbon dioxide adsorption on Illite. *Energy Fuels* 2016;30(12):10643–52.
- [37] Jeon PR, Choi J, Yun TS, Lee C-H. Sorption equilibrium and kinetics of CO<sub>2</sub> on clay minerals from subcritical to supercritical conditions: CO<sub>2</sub> sequestration at nanoscale interfaces. *Chem Eng J* 2014;255:705–15.
- [38] Kadoura A, Narayanan Nair AK, Sun S. Adsorption of carbon dioxide, methane, and their mixture by montmorillonite in the presence of water. *Microporous Mesoporous Mater* 2016;225:331–41.
- [39] Wang Q, Huang L. Molecular insight into competitive adsorption of methane and carbon dioxide in montmorillonite: Effect of clay structure and water content. *Fuel* 2019;239:32–43.
- [40] He M-C, Zhao J, Li Y. First principles ab initio study of CO<sub>2</sub> adsorption on the kaolinite (001) surface. *Clays Clay Miner* 2014;62(2):153–60.
- [41] Hu X, Deng H, Lu C, Tian Y, Jin Z. Characterization of CO<sub>2</sub>/CH<sub>4</sub> competitive adsorption in various clay minerals in relation to shale gas recovery from molecular simulation. *Energy Fuels* 2019;33(9):8202–14.
- [42] Liu Y, Hou J. Selective adsorption of CO<sub>2</sub>/CH<sub>4</sub> mixture on clay-rich shale using molecular simulations. *J CO<sub>2</sub> Util* 2020;39:101143.
- [43] Zhang M, Jin Z. Molecular simulation on CO<sub>2</sub> adsorption in partially water-saturated kaolinite nanopores in relation to carbon geological sequestration. *Chem Eng J* 2022;450:138002.
- [44] Day-Stirrat RJ, Hillier S, Nikitin A, Hofmann R, Mahood R, Mertens G. Natural gamma-ray spectroscopy (NGS) as a proxy for the distribution of clay minerals and bitumen in the Cretaceous McMurray Formation, Alberta. *Canada Fuel* 2021;288:119513.

- [45] Hong H, Cheng F, Yin K, Churchman GJ, Wang C. Three-component mixed-layer illite/smectite/kaolinite (I/S/K) minerals in hydromorphic soils, south China. *Am Mineral* 2015;100(8–9):1883–91.
- [46] Rahrostaqim M, Sahimi M. Molecular dynamics simulation of hydration and swelling of mixed-layer clays. *J Phys Chem C* 2018;122(26):14631–9.
- [47] Rahrostaqim M, Sahimi M. Molecular dynamics simulation of hydration and swelling of mixed-layer clays in the presence of carbon dioxide. *J Phys Chem C* 2019;123(7):4243–55.
- [48] Środoń J. Nature of mixed-layer clays and mechanisms of their formation and alteration. *Annu Rev Earth Planet Sci* 1999;27(1):19–53.
- [49] Ulian G, Moro D, Valdrè G. Water adsorption behaviour on (001) pyrophyllite surface from ab initio Density Functional Theory simulations. *Appl Clay Sci* 2021; 212:106221.
- [50] Lee JH, Guggenheim S. Single crystal X-ray refinement of pyrophyllite-1 Tc. *Am Mineral* 1981;66(3–4):350–7.
- [51] Wardle R, Brindley GW. The crystal structures of pyrophyllite, 1Te, and of its dehydroxylate. *Am Mineral* 1972;57(5–6):732–50.
- [52] Pan ZJ, Connell LD, Camilleri M, Connnelly L. Effects of matrix moisture on gas diffusion and flow in coal. *Fuel* 2010;89(11):3207–17.
- [53] Humphrey W, Dalke A, Schulten K. VMD: Visual molecular dynamics. *J Mol Graph* 1996;14(1):33–8.
- [54] Cygan RT, Liang JJ, Kalinichev AG. Molecular models of hydroxide, oxyhydroxide, and clay phases and the development of a general force field. *J Phys Chem B* 2004; 108(4):1255–66.
- [55] Cygan RT, Romanov VN, Myshakin EM. Molecular simulation of carbon dioxide capture by montmorillonite using an accurate and flexible force field. *J Phys Chem C* 2012;116(24):13079–91.
- [56] Berendsen H, Grigera J, Straatsma T. The missing term in effective pair potentials. *J Phys Chem* 1987;91(24):6269–71.
- [57] Peng Z, Ewig CS, Hwang M-J, Waldman M, Hagler AT. Derivation of class II force fields. 4. van der Waals parameters of alkali metal cations and halide anions. *J Phys Chem A* 1997;101(39):7243–52.
- [58] Frenkel D, Smit B. Understanding molecular simulation: from algorithms to applications. Elsevier; 2001.
- [59] Plimpton S. Fast parallel algorithms for short-range molecular dynamics. *J Comput Phys* 1995;117(1):1–19.
- [60] Verlet L. Computer“ experiments” on classical fluids. I. Thermodynamical properties of Lennard-Jones molecules. *Phys Rev* 1967;159(1):98–103.
- [61] Hoover WG. Canonical dynamics: Equilibrium phase-space distributions. *Phys Rev A* 1985;31(3):1695–7.
- [62] Peng D-Y, Robinson DB. A new two-constant equation of state. *Ind Eng Chem Fundam* 1976;15(1):59–64.
- [63] Darden T, York D, Pedersen L. Particle mesh Ewald: An N-log(N) method for Ewald sums in large systems. *J Chem Phys* 1993;98(12):10089–92.
- [64] Wallace WE. ‘Mass Spectra’ in NIST Chemistry WebBook, NIST Standard Reference Database Number 69, 2018.
- [65] Sarrade SJ, Rios GM, Carles M. Supercritical CO<sub>2</sub> extraction coupled with nanofiltration separation: Applications to natural products. *Sep Purif Technol* 1998;14(1–3):19–25.
- [66] Sudibandriyo M, Pan Z, Fitzgerald JE, Robinson RL, Gasem KAM. Adsorption of methane, nitrogen, carbon dioxide, and their binary mixtures on dry activated carbon at 318.2 K and pressures up to 13.6 MPa. *Langmuir* 2003;19(13):5323–31.
- [67] Willems TF, Rycroft CH, Kazi M, Meza JC, Haranczyk M. Algorithms and tools for high-throughput geometry-based analysis of crystalline porous materials. *Microporous Mesoporous Mater* 2012;149(1):134–41.
- [68] Fitzgerald JE, Pan Z, Sudibandriyo M, Robinson JRL, Gasem KAM, Reeves S. Adsorption of methane, nitrogen, carbon dioxide and their mixtures on wet Tiffany coal. *Fuel* 2005;84(18):2351–63.
- [69] Ozawa S, Kusumi S, Ogino Y. Physical adsorption of gases at high pressure. IV. An improvement of the Dubinin—Astakhov adsorption equation. *J Colloid Interface Sci* 1976;56(1):83–91.
- [70] Gasparik M, Ghanizadeh A, Bertier P, Gensterblum Y, Bouw S, Krooss BM. High-pressure methane sorption isotherms of black shales from the Netherlands. *Energy Fuels* 2012;26(8):4995–5004.
- [71] Langmuir I. The constitution and fundamental properties of solids and liquids. Part I. Solids. *J Am Chem Soc* 1916;38(11):2221–95.
- [72] Liu D, Yuan P, Liu H, Li T, Tan D, Yuan W, et al. High-pressure adsorption of methane on montmorillonite, kaolinite and illite. *Appl Clay Sci* 2013;85:25–30.
- [73] Zhu H, Zhang Y, Fang S, Huo Y, Wang H, Cheng G. Methane adsorption influence and diffusion behavior of coking coal macromolecules under different moisture contents. *Energy Fuels* 2020;34(12):15920–35.
- [74] Sakurovs R, Day S, Weir S, Duffy G. Application of a modified Dubinin-Radushkevich equation to adsorption of gases by coals under supercritical conditions. *Energy Fuels* 2007;21(2):992–7.
- [75] Jin Z, Firoozabadi A. Methane and carbon dioxide adsorption in clay-like slit pores by Monte Carlo simulations. *Fluid Phase Equilib* 2013;360:456–65.
- [76] Nicholson W, Nicholson D, Parsonage NG. Computer simulation and the statistical mechanics of adsorption. Academic Press; 1982.
- [77] Palace Carvalho AJ, Ferreira T, Estevão Candeias AJ, Prates Ramalho JP. Molecular simulations of nitrogen adsorption in pure silica MCM-41 materials. *J Mol Struct THEOCHEM* 2005;729(1):65–9.
- [78] Billemont P, Coasne B, De Weireld G. Adsorption of carbon dioxide, methane, and their mixtures in porous carbons: effect of surface chemistry, water content, and pore disorder. *Langmuir* 2013;29(10):3328–38.
- [79] Ruthven DM. Principles of Adsorption and Adsorption Processes. John Wiley & Sons; 1984.
- [80] Wu H, Jin Z, Xu X, Zhao S, Liu H. Effect of competitive adsorption on the deformation behavior of nanoslit-confined carbon dioxide and methane mixtures. *Chem Eng J* 2022;431:133963.
- [81] Hao Y, Yuan L, Li P, Zhao W, Li D, Lu D. Molecular simulations of methane adsorption behavior in illite nanopores considering basal and edge surfaces. *Energy Fuels* 2018;32(4):4783–96.
- [82] Li J, Li B, Gao Z, Zhang Y, Wang B. Adsorption behavior, including the thermodynamic characteristics of wet shales under different temperatures and pressures. *Chem Eng Sci* 2021;230:116228.
- [83] Ammendola P, Raganati F, Chirone R. CO<sub>2</sub> adsorption on a fine activated carbon in a sound assisted fluidized bed: Thermodynamics and kinetics. *Chem Eng J* 2017; 322:302–13.
- [84] Zhang G, Al-Saidi WA, Myshakin EM, Jordan KD. Dispersion-corrected density functional theory and classical force field calculations of water loading on a pyrophyllite (001) surface. *J Phys Chem C* 2012;116(32):17134–41.
- [85] Zhou X-Y, Zhu J-H, Wu H-H. Molecular dynamics studies of the grain-size dependent hydrogen diffusion coefficient of nanograined Fe. *Int J Hydrogen Energy* 2021;46(7):5842–51.
- [86] Yang W, Zouaii A. Capture and sequestration of CO<sub>2</sub> in the interlayer space of hydrated calcium Montmorillonite clay under various geological burial depth. *Phys A* 2016;449:416–25.
- [87] Andrews D, Scholes G, Wiederrecht G. Comprehensive nanoscience and technology. New York: Academic Press; 2010.
- [88] Luza A, Chandler D. Structure and hydrogen bond dynamics of water–dimethyl sulfoxide mixtures by computer simulations. *J Chem Phys* 1993;98(10):8160–73.
- [89] Wang J, Kalinichev AG, Kirkpatrick RJ. Asymmetric hydrogen bonding and orientational ordering of water at hydrophobic and hydrophilic surfaces: a comparison of water/vapor, water/talc, and water/mica interfaces. *J Phys Chem C* 2009;113(25):11077–85.
- [90] Xu H, Yu H, Fan J, Zhu Y, Wang F, Wu H. Two-phase transport characteristic of shale gas and water through hydrophilic and hydrophobic nanopores. *Energy Fuels* 2020;34(4):4407–20.
- [91] Xu J, Zhan S, Wang W, Su Y, Wang H. Molecular dynamics simulations of two-phase flow of n-alkanes with water in quartz nanopores. *Chem Eng J* 2022;430: 132800.